Check for updates

Quaternary morpholinium-mediated defect control in high-performance perovskite solar cells

Shengnan Wang,[a] Ranran Xu,[a] Fengqiao Xu,[a] Weidong Lin,[b] Yongbing Lou, [ID] *[a] Zhixiao Qin*[c] and Taiyang Zhang*[b]

Although perovskite solar cells (PSCs) have achieved impressive efficiency advancements, their surface-dominated defects and poor environmental robustness still restrict device performance and durability. Here, we develop a multifunctional morpholinium-based quaternary ammonium salt, 4-ethyl-4-methylmorpholinium bromide (EMMorBr), as an efficient post-treatment molecule to modulate perovskite surface chemistry and interfacial energetics. Benefiting from its unique molecular configuration, EMMorBr enables dual-site defect passivation through the strong coordination between its electron-rich oxygen atom and under-coordinated Pb^{2+}, as well as electrostatic interactions between quaternary ammonium cations and halide vacancies. Meanwhile, hydrogen bonding interactions restrain organic cation vacancy formation, leading to suppressed non-radiative recombination and improved interfacial charge extraction. The resulting films exhibit enhanced crystallinity, reduced trap density, and more favorable energy-level alignment. As a consequence, the EMMorBr-modified inverted PSCs achieve a champion power conversion efficiency of 26.14% with negligible hysteresis. Moreover, the devices display remarkable environmental durability. This work offers a rational molecular-engineering strategy toward high-efficiency and stable PSCs by leveraging quaternary onium salt chemistry.

1 Introduction

Organic–inorganic hybrid metal halide perovskite solar cells (PSCs) continue to attract extensive attention due to their high power conversion efficiency (PCE) and other advantages such as solution processability, low cost, and flexible fabrication processes.[1–3] To date, single-junction PSCs have achieved a certified PCE of 27.2%, rivaling the performance of the most advanced silicon-based solar cells.[4] Nevertheless, this value remains substantially below the theoretical Shockley–Queisser limit (~33%).[5,6] Moreover, the commercialization of PSCs is limited by reduced stability during prolonged operation.[7] These challenges primarily originate from the inherent characteristics of perovskite crystallization kinetics during solution processing, where rapid crystallization inevitably leads to various complex defects.[8,9] Studies reveal that defects in perovskite films are predominantly concentrated at surfaces and interfaces, exhibiting a density 1–2 orders of magnitude higher than that in the bulk.[10–12] Surface defects readily act as deep trap states that dominate nonradiative recombination, severely impairing charge carrier extraction and thereby reducing device

efficiency.[13] Simultaneously, these defect sites facilitate reactions with ambient moisture and oxygen, triggering the decomposition of the perovskite lattice and accelerating device degradation.[14,15] Therefore, developing effective strategies to suppress surface defects and enhance the interfacial properties of perovskite films is crucial for the industrialization of PSCs.

Currently, developing and optimizing surface passivation techniques is recognized as an effective approach for enhancing the performance and stability of PSCs.[16] Various passivation agents have been developed to mitigate interfacial defects, primarily including Lewis bases,[17,18] polymers,[19,20] low-dimensional perovskites[21,22] and organic salts.[23,24] Compared with other interfacial materials, organic halide salts demonstrate greater potential due to their dual capability to passivate both positively and negatively charged defects in perovskite films.[24] While various categories of organic ammonium salts can achieve chemical passivation (e.g., phenethylammonium iodide and piperazinium iodide), their ammonium cations tend to undergo deprotonation and form organic amines, particularly under illumination and elevated temperatures, leading to device instability and performance degradation.[25–27] In contrast, quaternary ammonium cations, where reactive protons are replaced by lipophilic alkyl groups, demonstrate superior thermal and chemical stability.[28] Song et al. found that perovskites with quaternary ammonium cations exhibit lower surface structural defects and superior thermal stability compared to those with primary ammonium cations.[29] Furthermore, due to

[a]School of Chemistry and Chemical Engineering, Southeast University, Nanjing 211189, China. E-mail: lou@seu.edu.cn

[b]School of Chemical and Environmental Engineering, Shanghai Institute of Technology, 100 Haiquan Road, Shanghai 201418, China. E-mail: taiyangzhang@sit.edu.cn

[c]Shanghai Pvsktech Co., Ltd., Shanghai, China. E-mail: zhixiao.qin@pvsktech.com

their larger steric hindrance, quaternary ammonium cations only passivate surface and interfacial defects without penetrating into the perovskite lattice, thereby avoiding charge transport issues associated with the formation of 2D phases.[30] The absence of lone pair electrons on the nitrogen in quaternary ammonium cations prevents it from coordinating with Pb^{2+} or forming hydrogen bonds with FA^+/MA^+, thereby weakening its defect passivation efficacy.[31–33] Moreover, conventional quaternary ammonium salts may fail to precisely modulate the energy-level alignment between the perovskite and the charge transport layer, thereby limiting the charge extraction efficiency.[34,35] Therefore, the molecular structure of quaternary ammonium salts should be rationally designed to ensure both effective defect passivation and interfacial energy level optimization for improved performance in PSCs.

Herein, we introduce a novel multifunctional morpholinium-based quaternary ammonium salt, 4-ethyl-4-methylmorpholinium bromide (EMMorBr), as a post-treatment molecule to modulate perovskite film quality. We propose that the ammonium group and bromide ions in EMMorBr passivate negatively and positively charged defects, respectively. The electron-rich O atom on the morpholine ring effectively passivates under-coordinated Pb^{2+} defects at surfaces or grain boundaries, while simultaneously suppressing the formation of organic cation vacancies through hydrogen bonding ($N–H\cdots O$) with FA^+. The EMMorBr-modified perovskite films demonstrate improved surface smoothness, uniform surface potential, and ideal energy level alignment. As a result, the EMMorBr-modified $FA_{0.85}MA_{0.1}Cs_{0.05}PbI_3$-based inverted PSCs achieved a PCE of 26.14%. More notably, the EMMorBr-modified device demonstrated outstanding stability. After 1500 h of aging in either a N_2 atmosphere or ambient air at 30–40% relative humidity, the unencapsulated PSCs retained 98% and 88% of their initial PCE, respectively.

2 Results and discussion

Fig. 1a shows the chemical structure and electrostatic potential (ESP) of EMMorBr. As a quaternary onium salt, EMMorBr consists of a morpholine ring and a quaternary ammonium
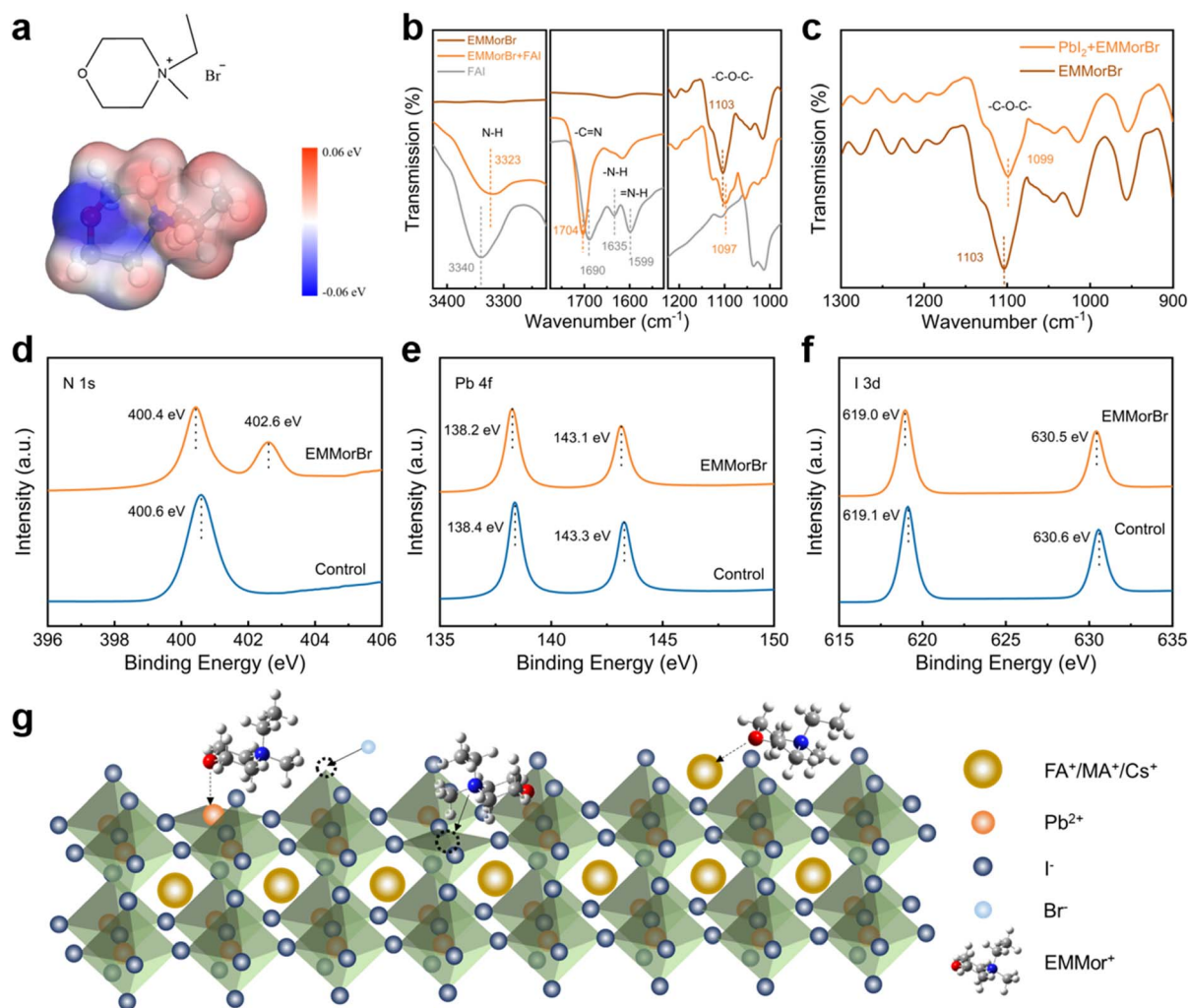

Fig. 1 (a) Molecular structure and calculated ESP profiles of EMMorBr. (b) FTIR spectra of EMMorBr powder and a mixture of EMMorBr and FAI. (c) FTIR spectra of EMMorBr with and without PbI_2. (d) N 1s, (e) Pb 4f and (f) I 3d XPS spectra of control and EMMorBr-modified perovskite films. (g) Schematic diagram of the interaction between EMMorBr and the perovskite.

group. The electron-rich center is localized around the O atom and the electron-deficient region is centered on the NR_4 group, creating a strong dipole moment. The quaternary ammonium cation can electrostatically interact with uncoordinated I^- anions, effectively suppressing ion migration and defect formation. Additionally, due to the Lewis base properties of the morpholine ring, the O atom can repair undercoordinated Pb^{2+} defects through coordinate bonding.

The chemical interaction between EMMorBr and the perovskite framework is first evidenced *via* Fourier transform infrared (FTIR) spectroscopy. As shown in Fig. 1b, after the interaction with EMMorBr, the N–H stretching peak of FAI shifted from 3340 cm^{-1} to 3323 cm^{-1}, and the N–H bending band at 1599 cm^{-1} exhibited attenuation. In addition, the shifts of the C=N stretching peak of FAI from 1690 cm^{-1} to 1704 cm^{-1} and the C–O stretching peak of EMMorBr from 1103 cm^{-1} to 1099 cm^{-1} collectively indicate the formation of hydrogen bonds between EMMorBr and FA^+ cations.[36,37] Similarly, after the interaction with PbI_2, the C–O stretching peak in EMMorBr shifted from 1103 cm^{-1} to 1097 cm^{-1}, indicating the formation of Pb–O coordinate bonding (Fig. 1b and c).[38,39] Therefore, EMMorBr molecules can form strong molecular interactions with both the inorganic framework and organic compounds. To further demonstrate the interaction between EMMorBr and perovskite, XPS measurements were conducted (Fig. S1). No Br signal was observed in the pristine perovskite film. In contrast, a distinct Br 3d peak at ≈ 70.56 eV is evident in the EMMorBr-modified film, confirming the presence of bromide ions. As shown in Fig. 1d, a new N 1s signal at 402.6 eV appeared in the EMMorBr film, which could be attributed to the N signal of quaternary ammonium ions, confirming that EMMorBr was

attached to the surface of the perovskite films.[40] Additionally, the N 1s peak of FA^+ shifted from 400.6 eV to 400.4 eV after the EMMorBr modification, further confirming the formation of N–H⋯O hydrogen bonds between FA^+ and the C–O–C functional groups in EMMorBr.

The Pb $4f_{5/2}$ and Pb $4f_{7/2}$ peaks at 143.8 eV and 138.9 eV also shift to lower binding energies of 143.6 eV and 138.7 eV after EMMorBr modification (Fig. 1e), confirming the interaction between undercoordinated Pb^{2+} and EMMorBr.[41] Such a shift can be attributed to the dual-site passivation capability of EMMorBr, wherein Br^- ions compensate for halide vacancies or bind with exposed Pb^{2+}, while the electron-rich O atoms simultaneously coordinate with undercoordinated Pb^{2+}, collectively reducing defect states at grain boundaries. Similarly, the I $3d_{3/2}$ and I $3d_{5/2}$ peaks of the control film shifted from 630.6 eV and 619.1 eV to 630.5 eV and 619.0 eV in the EMMorBr-modified film (Fig. 1f). This shift is attributed to an increased electron cloud density around iodine atoms, which indicates effective suppression of iodine vacancy defects at the perovskite grain boundaries.[42] The interaction mechanisms between EMMorBr and perovskite components are shown in Fig. 1g.

The effects of EMMorBr treatment on the perovskite films were further investigated. Scanning electron microscopy (SEM) images revealed that the EMMorBr-modified perovskite film exhibited a smoother and more uniform surface compared to the control sample (Fig. 2a and b). Concurrently, significantly reduced excess PbI_2 aggregation and increased grain size were observed in the EMMorBr-modified films (Fig. S2). This phenomenon can likely be attributed to the strong interaction between EMMorBr and the perovskite, which promotes the coalescence of small grains into larger ones *via* Ostwald
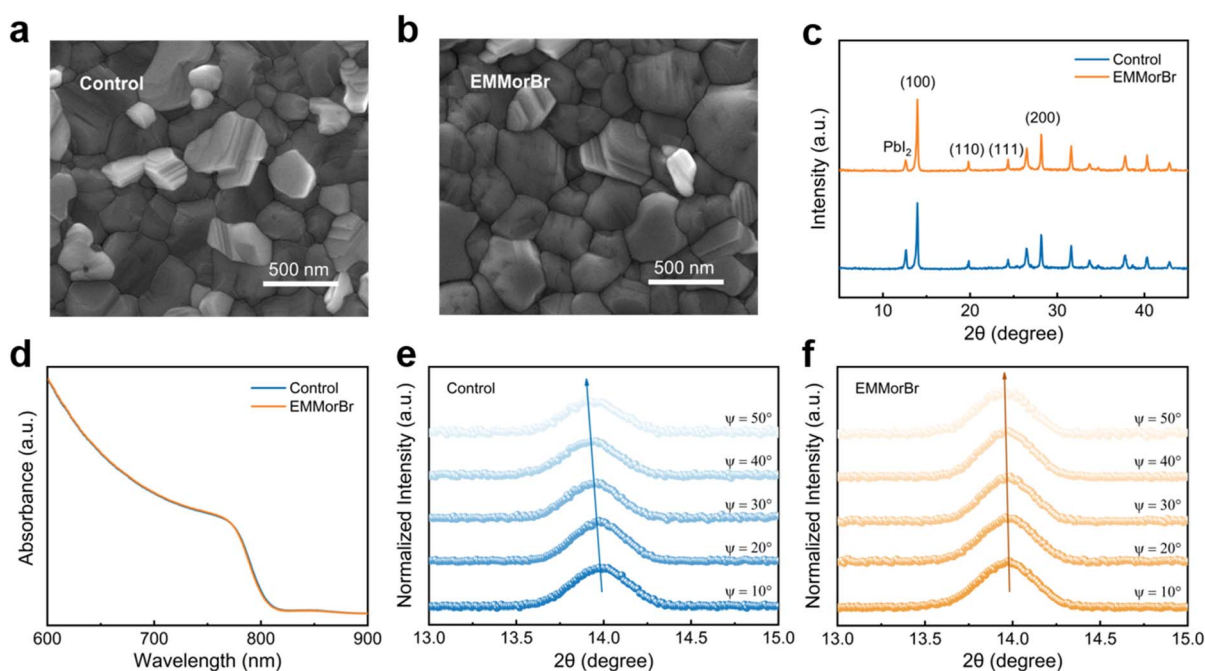
Fig. 2 (a and b) Top-view SEM images of the control and EMMorBr-modified perovskite films. (c) XRD patterns of perovskite films. (d) UV-vis spectra of perovskite films with and without EMMorBr modification. (e and f) GIXRD spectrum of the (100) plane at different tilt angles for the control and EMMorBr-modified perovskite films.

Ripening.[43,44] Atomic force microscopy (AFM) analysis reveals that the roughness of the control is 20.8 nm, while that of perovskite films modified with EMMorBr is 16.5 nm (Fig. S3), indicating that EMMorBr treatment could obtain higher-quality perovskite films with reduced surface roughness. A smoother surface facilitates better contact with the electron transport layer (ETL), enhancing electron extraction and transfer.[45] X-ray diffraction (XRD) analysis (Fig. 2c and S4) shows that EMMorBr modification does not alter the perovskite crystal phase. Meanwhile, the PbI_2 diffraction signal is markedly reduced, indicating effective removal of residual PbI_2 through its interaction with EMMorBr. The UV-vis absorption spectra reveal that EMMorBr modulation has a negligible impact on the bandgap and absorbance of the films (Fig. 2d and S5), confirming that the optical properties remain largely unaffected.[46] To determine whether EMMorBr acts exclusively at the top surface or diffuses into the bulk, XPS depth profiling was performed on the EMMorBr-modified perovskite film to analyze the elemental composition from the surface to deeper layers (Fig. S6). The results clearly indicate that the Br 3d and N 1s

signals become negligible after etching the film to a depth of 20 nm, whereas the peak intensities of Pb 4f and I 3d show no significant change.[47] Subsequently, the residual stress in the perovskite films was examined by grazing incidence X-ray diffraction (GIXRD). As shown in Fig. 2e and f, the (100) diffraction peak of the control film exhibits a significant shift toward lower angles as the tilt angle increases from 10° to 50°, suggesting the presence of residual stress at the surface and interface.[48] In contrast, the (100) diffraction peak of the EMMorBr-modified perovskite film shows minimal shift as the incident angle increases, demonstrating effective interfacial stress relaxation. Such a phenomenon is likely attributed to the coordination and hydrogen bonding interactions between EMMorBr and the perovskite lattice, which effectively stabilize the crystalline structure, thereby reducing the trap density in the modified perovskite films.[49]

To gain better insight into the carrier recombination dynamics at the interface, steady-state photoluminescence (PL), PL mapping, and time-resolved photoluminescence (TRPL) spectra were investigated. As shown in Fig. S7, the emission
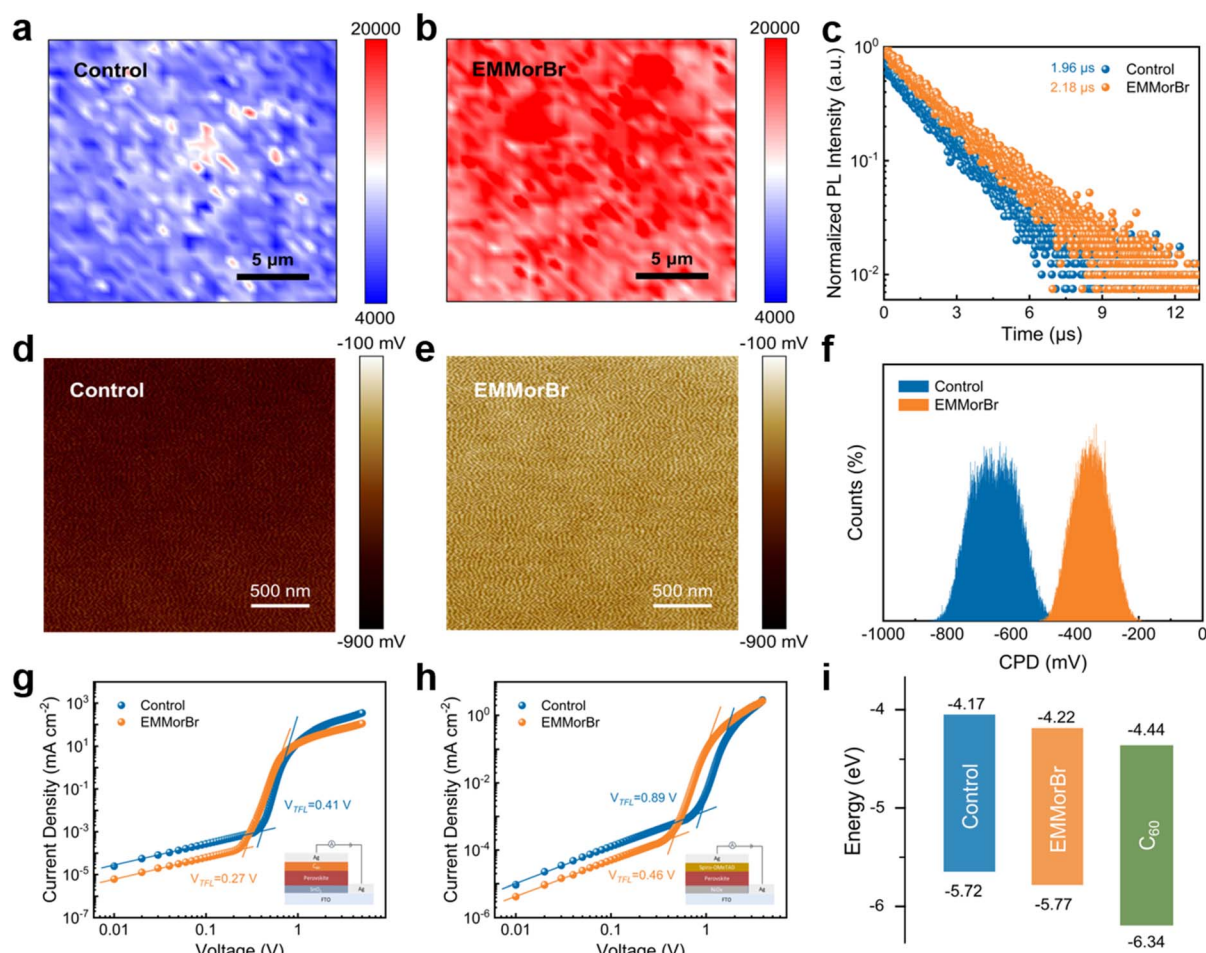

Fig. 3 (a and b) PL mapping patterns of control and EMMorBr-modified perovskite films. (c) TRPL spectra of the control and EMMorBr-modified perovskite films deposited on nonconductive glass. (d and e) KPFM measurement of the perovskite films with and without EMMorBr modification. (f) CPD statistical distributions derived from the KPFM images. (g) $J–V$ curves of the electron-only devices based on ITO/SnO_2/perovskite/C_{60}/Ag structures and (h) the hole-only devices based on ITO/NiO_x/perovskite/spiro-OMeTAD/Ag structures. (i) Energy level diagram of perovskite and C_{60}.

intensity of the EMMorBr-modified film at around 800 nm was significantly higher than that of the control film. Moreover, the EMMorBr-modified perovskite film also shows more uniform and higher PL intensity in PL mapping patterns (Fig. 3a, b and S8), indicating a significant reduction in nonradiative recombination at the surface. The TRPL results show that the carrier lifetime in EMMorBr-modified films increased significantly, with the average lifetime rising from 1.96 μs to 2.18 μs compared to the control (Fig. 3c and Table S1).[50] The prolonged carrier lifetime and enhanced PL intensity in the modified perovskite films indicated the excellent defect healing function of EMMorBr, which minimized nonradiative recombination losses and thereby enhanced device photovoltaic performance.[51] Furthermore, EMMorBr-modified films also demonstrate higher contact potential difference (CPD) values (from −651 mV to −342 mV), indicating a decrease in the work function of the perovskite top surface (Fig. 3d and e).[52] It is thus evident that the introduction of EMMorBr renders the perovskite surface more biased toward n-type semiconductors, which further promotes efficient electron extraction and hole blocking.[53,54] Meanwhile, EMMorBr-modified perovskite displays a more uniform surface potential distribution (Fig. 3f), implying a reduction in defect density, which will enhance the charge transfer efficiency at the electron transport layer interface.[33]

In order to quantitatively evaluate the passivation effects of EMMorBr, the trap state density of the perovskite films was determined by the space charge limited current (SCLC) method.[55] Fig. 3g and h respectively show dark current–voltage (J–V) curves of the electron-only device (ITO/SnO$_2$/perovskite/C$_{60}$/Ag) and the hole-only device (ITO/NiO$_X$/perovskite/spiro-OMeTAD/Ag). According to the formula $N_t = 2\varepsilon_0\varepsilon_r V_{TFL}/qL^2$, the trap density value is positively correlated with the V_{TFL} value.[56] As for the electron-only devices, the defect density of the EMMorBr-modified film decreased from 1.54×10^{16} cm^{-3} to 0.96×10^{16} cm^{-3} compared with the control film. Similarly, for hole-only devices, the defect density decreased from 3.16×10^{16} cm^{-3} to 1.70×10^{16} cm^{-3}. These results quantitatively confirm that EMMorBr effectively passivates diverse defects on the perovskite surface.
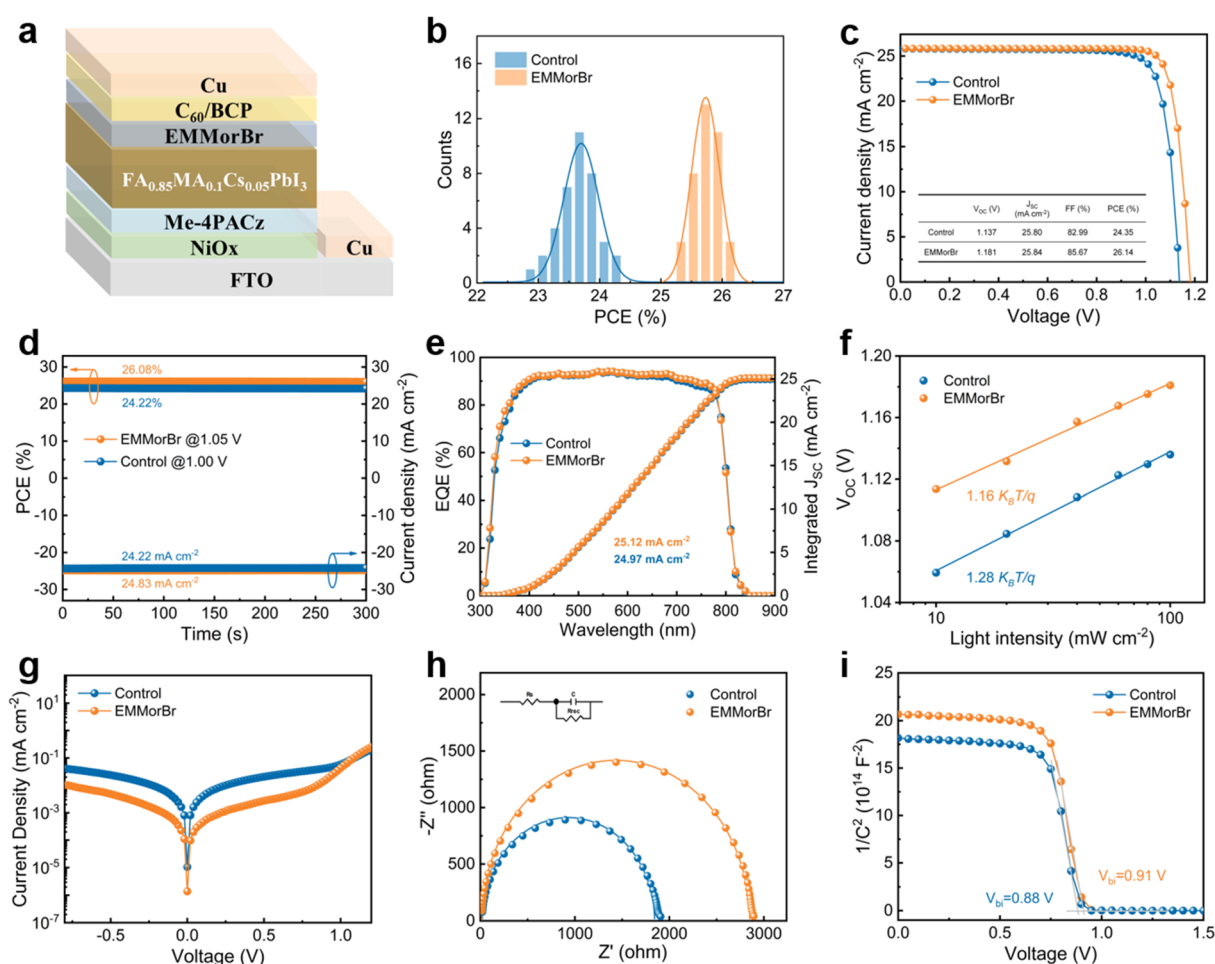

Fig. 4 (a) Schematic diagram of the device structure. (b) Histogram for PCE distribution from devices with and without EMMorBr modification. (c) Steady-state efficiency at the maximum power point for PSCs. (d) J–V curves of control and EMMorBr-modified devices with champion performance. (e) EQE spectra and corresponding integrated current density of the champion device. (f) The dependence of V_{OC} on light intensity. (g) Dark state J–V curve. (h) EIS for devices in the dark with 1 V bias voltage. (i) Mott–Schottky (M–S) curves of EMMorBr-modified and control devices.

As revealed by ultraviolet photoelectron spectroscopy (UPS), we can conclude that the Fermi level of the EMMorBr-modified perovskite film shifted upward from −4.38 eV to −4.29 eV, compared to the control perovskite film (Fig. S9). Combined with the bandgap values determined from UV-vis, the energy level positions of both the control and modified films can be calculated (Fig. 3i and S10). As shown in the corresponding schematic diagram of the bandgap structure, the conduction band minimum (CBM) of the perovskite film shifts downward from −4.17 to −4.22 eV after EMMorBr modulation. This trend aligns with the KPFM results and leads to a reduced energy offset between the CBM of the perovskite film and that of C_{60}. The reduced energy level mismatch facilitates interfacial electron extraction and transfer.[57,58]

We fabricated inverted PSCs with the device structure of $FTO/NiO_x/Me-4PACz/Perovskite/EMMorBr/C_{60}/BCP/Cu$. The schematic device architecture is presented in Fig. 4a, and the corresponding structural layers were confirmed by the cross-sectional SEM image in Fig. S11. After optimization (Fig. S12), the champion efficiency of the EMMorBr-modified device is 26.14%, while the control device is 24.35% (Fig. 4b and c). The EMMorBr-modified PSCs exhibit reduced hysteresis (Fig. S13 and Table S2), as the hysteresis index (HI) value is only 1.03%, much lower than that of the control devices (5.26%). The corresponding stable power output (SPO) shown in Fig. 4d indicates that the EMMorBr-modified device obtained a stable output of 26.08%, while only 24.22% PCE was achieved for the control. The EMMorBr group achieved an average PCE of 25.75%, significantly higher than the 23.67% of the control group, demonstrating the superior reproducibility of the EMMorBr-modified devices. Fig. 4e presents the external quantum efficiency (EQE) spectra of both the control and EMMorBr-modified devices. The integrated current density of 25.12 mA cm^{-2} is higher than that of the control device (24.97 mA cm^{-2}), which is consistent with the current density of the J–V curve. The improvement in the PCE of the passivated devices is primarily attributed to the enhanced V_{OC} and FF (Fig. S14), which can be primarily ascribed to the reduction of interface defects and the optimization of energy band alignment, coordination between EMMorBr and free ions and the suppression of non-radiative recombination.[59] As shown in the linear correlation between V_{OC} and light intensity (Fig. 4f), the ideal factor of EMMorBr-modified devices was determined to be 1.16 by slope fitting, which is significantly lower than the 1.28 of control devices.[60] Furthermore, as depicted in Fig. 4g, the dark current of the EMMorBr-modified device was much lower than that of the control sample (1.39×10^{-6} vs. 1.04×10^{-5} mA cm^{-2}). Electrochemical impedance spectroscopy (EIS) measurements were conducted on both control and EMMorBr-modified devices (Fig. 4h) to investigate the carrier recombination behavior. Compared with the control device, the EMMorBr-modified device exhibited remarkably decreased series resistance (R_S) and improved recombination resistance (R_{rec}) at open circuit voltage (1 V), indicating rapid charge transfer and reduced carrier recombination (Table S3). In addition, Mott–Schottky analysis revealed that the device modified with EMMorBr obtained a built-in potential (V_{bi}) of

0.91 V (Fig. 4i), which was higher than that of the control device (0.88 V). This is consistent with the increase in V_{OC} of the EMMorBr-modified device, which further proves that EMMorBr modification can effectively reduce defect density and optimize energy levels.[10,61]

The effect of EMMorBr modification on the long-term stability of PSCs was further investigated. Contact angle tests revealed that the water contact angle on the EMMorBr-modified perovskite film increased from 55.7° to 73.3°, indicating a notable improvement in surface hydrophobicity (Fig. 5a).[62] The EMMorBr-modified film maintained its black perovskite phase morphology even under harsh aging conditions in ambient air at 80% relative humidity (RH) for 80 d (Fig. 5b). Conversely, the control film underwent a gradual yellowing process with aging, indicating phase transition and decomposition of the perovskite material. We also tracked the evolution of the UV-vis absorption spectrum during aging. As shown in Fig. 5c, the absorption spectrum of the control film deviated significantly, indicating the loss of photoactivity. In contrast, the EMMorBr-modified film showed minimal spectral changes with only a slight reduction in absorption after 80 d. The hydrophobic methyl and ethyl branched chains of EMMorBr can form a dense hydrophobic protective layer on the perovskite surface, significantly enhancing the hydrophobicity of the perovskite. This is likely the reason for the superior stability of the EMMorBr-modified film under high-humidity conditions.

The long-term stability of PSCs under thermal stress is a critical factor for practical applications. Therefore, we further investigated the stability of the perovskite films under high-temperature aging conditions. After continuously heating the samples in a N_2 glovebox at 85 °C for 40 days, a significantly enhanced PbI_2 diffraction peak at 12.7° is clearly observed in the XRD pattern of the control film (Fig. 5d). In contrast, the PbI_2 diffraction peak is markedly suppressed in the EMMorBr-modified film (Fig. 5e). This demonstrates that the EMMorBr-modified perovskite film possesses superior thermal stability. This enhancement in thermal stability can be attributed to the ability of EMMorBr to stabilize the perovskite lattice and effectively suppress the escape of organic cations.[63] We performed further elemental analysis using XPS. Fig. S15 presents the N 1s spectra of the FA^+ cations for perovskite films before and after thermal aging. The results show that the integrated peak area for the control after aging is only 57.6% of its initial value, whereas the EMMorBr-modified sample retains 90.3% of its initial peak area after 40 d. This directly demonstrates that FA^+ loss under thermal stress predominantly occurs on the surface of the control film.[64] Furthermore, under identical aging conditions, the signal intensity changes of the characteristic elements in the N 1s and Br 3d orbitals of EMMorBr molecules are negligible. This indicates that EMMorBr does not readily detach from the perovskite surface during the aging process. Near-surface elemental analysis confirms that the thermal degradation of the control perovskite initiates with the compositional loss of FA^+ driven by thermal stress. In contrast, this loss of organic components is significantly suppressed by EMMorBr passivation, leading to a substantial enhancement in the material's thermal structural stability.
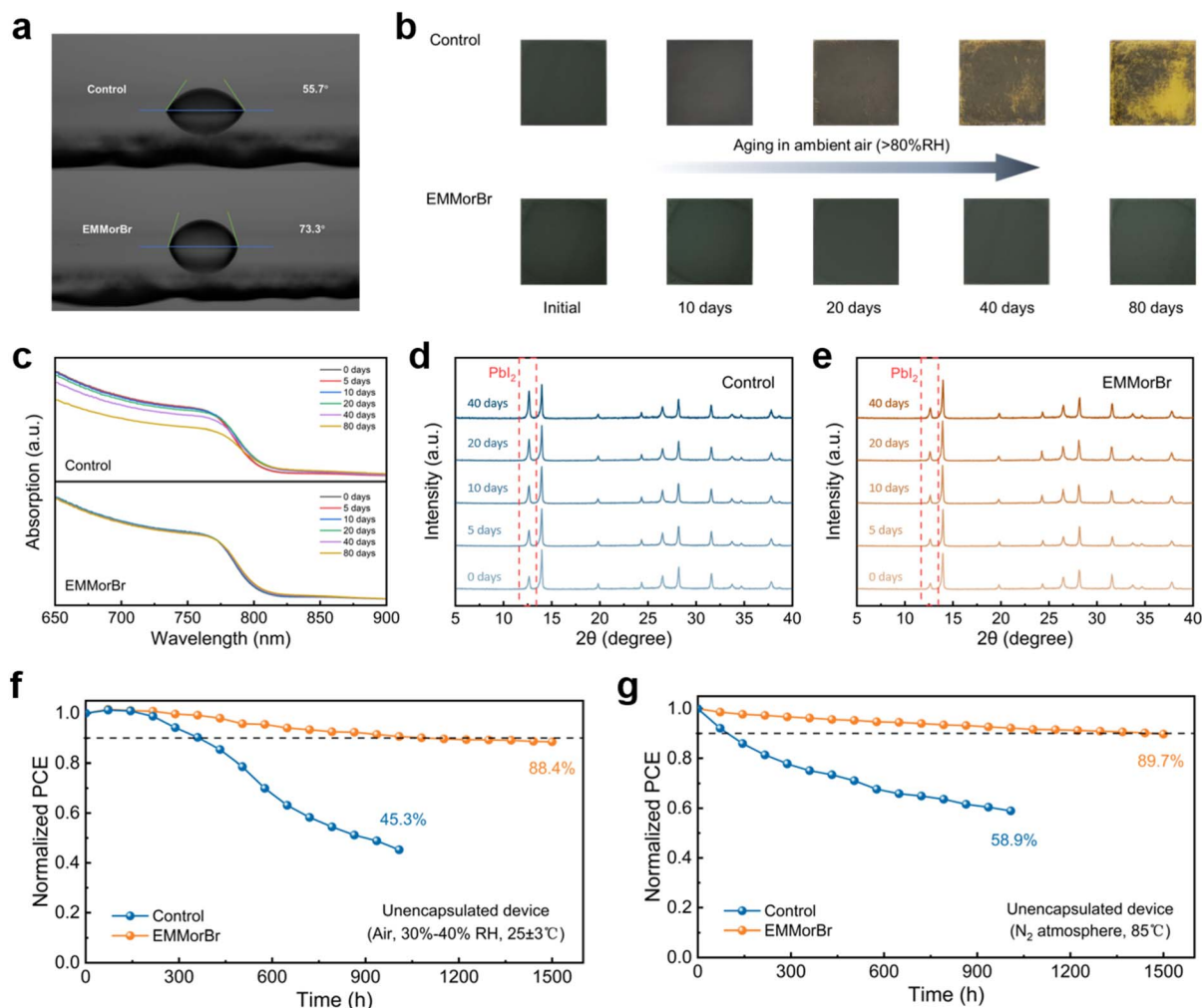
Fig. 5 (a) Water contact angle test of the control and DBI perovskite films. (b) Optical microscopy images of the control and EMMorBr-modified perovskite films aged in ambient air with 80% RH. (c) UV-vis absorption spectra evolution of perovskite films with and without EMMorBr modification after aging in 80% RH ambient air for 20 d. (d and e) Evolution of XRD spectra of perovskite films at 85 °C in a N$_2$ glovebox. (f) Evolution of PCE measured from the unencapsulated PSCs in ambient air with 30%–40% RH. (g) Evolution of PCE measured from the unencapsulated PSCs at 85 °C in a N$_2$ glovebox.

We performed long-term stability tests on devices under different conditions. As shown in Fig. 5f, the EMMorBr-modified PSCs retained over 88% of their initial PCE after 1500 h of aging in 30–40% RH ambient air, whereas the control devices maintained only 45% of their initial PCE after 1000 h. Furthermore, a direct comparison between EMMorBr and several common passivators in experiments was conducted (Fig. S16). The results demonstrate that EMMorBr not only achieves improved initial efficiency but also exhibits significantly superior long-term stability. These results directly demonstrate that EMMorBr modification endows the perovskite film with enhanced moisture resistance and oxidation resistance. Concurrently, to evaluate the long-term stability of EMMorBr under thermal stress, we performed aging tests on both the control and EMMorBr devices at 85 °C in a N$_2$ glovebox (Fig. 5g). The results show that the power output of the control devices rapidly decayed to below 60% after 1000 h, whereas the EMMorBr devices retained 89% of their initial power conversion

efficiency after 1500 h. We also placed these PSCs in a N$_2$-filled environment to simulate encapsulation conditions. As shown in Fig. S17, the EMMorBr-modified PSCs retained 98% of their initial PCE after 1500 h of aging in a N$_2$-filled glovebox, compared to only 78% for the control devices. Therefore, the introduction of EMMorBr as a perovskite surface modifier achieves an effective dual improvement for both PCE and long-term stability.

3 Conclusions

In summary, we successfully introduced a rationally designed morpholinium-based quaternary ammonium salt (EMMorBr) for perovskite surface passivation and interfacial defect suppression. EMMorBr simultaneously forms coordinate bonds with Pb^{2+}, electrostatic interactions with halide vacancies, and hydrogen bonds with FA$^+$, collectively eliminating deep traps and suppressing ion migration. This synergistic passivation not

only enhances film crystallinity and reduces trap density but also optimizes the energy-level alignment at the perovskite/electron-transport interface. Consequently, the modified inverted PSCs deliver a significantly improved PCE of 26.14%, together with greatly enhanced stability under both ambient and inert environments. Our findings highlight the critical role of molecular-structure engineering in passivating multi-type defects and constructing robust interfaces, paving a promising path for industrially viable high-performance PSCs.

Author contributions

S. W. conceived the idea, designed the overall experiments, and wrote the manuscript. S. W. and R. X. carried out the device fabrication and characterization under the supervision of T. Z. W. L., F. X., and T. Z. reviewed and revised the figures and manuscript content. Z. Q. contributed materials and analysis tools. W. L. and Y. L. provided helpful suggestions for data interpretation. T. Z. and Y. L. directed and supervised this project. All authors discussed the results and commented on the manuscript.

Conflicts of interest

The authors declare no competing financial interest.

Data availability

The data supporting this article have been included as part of the supplementary information (SI). Supplementary information: many further experimental details. See DOI: https://doi.org/10.1039/d5ta10578a.

Acknowledgements

References

1 C. Luo, Q. Zhou, K. Wang, X. Wang, J. He, P. Gao, C. Zhan, Z. Bi, W. Li, Y. Ma, W. Chen, Y. Hou, Z. Liu and Q. Zhao, *Nat. Mater.*, 2025, **24**, 1265–1272.

2 Y. Wang, C. Lu, M. Liu, C. Zhu, J. Zhang, S. Qin, Z. Liu, M. Liu, Y. Zhao, F. Wang, X. Li, L. Meng and Y. Li, *Nat. Photonics*, 2025, **19**, 985–991.

3 B. Zhou, M. Li, Q. Xiong, L. Zhang, S. Zhang, J. Sun, J. Tang and W. C. H. Choy, *Energy Environ. Sci.*, 2025, **18**, 8803–8814.

4 Z. Xiong, Q. Zhang, K. Cai, H. Zhou, Q. Song, Z. Han, S. Kang, Y. Li, Q. Jiang, X. Zhang and J. You, *Science*, 2025, **390**, 638–642.

5 H. Dong, J. Qu, S. Wang, D. Chen, W. Chai, W. Wang, W. Zhu, H. Xi, J. Zhang, X. Zhang, C. Zhang and Y. Hao, *Adv. Mater.*, 2025, **37**, e11111.

6 J. Tao, C. Zhao, Z. Wang, Y. Chen, L. Zang, G. Yang, Y. Bai and J. Chu, *Energy Environ. Sci.*, 2025, **18**, 509–544.

7 Q. Jiang, R. Tirawat, R. A. Kerner, E. A. Gaulding, Y. Xian, X. Wang, J. M. Newkirk, Y. Yan, J. J. Berry and K. Zhu, *Nature*, 2023, **623**, 313–318.

8 W. Zhang, C. Xing, W. Song, J. Xie, H. Guan, J. Shan, J. Zhu, M. Yang and Z. Ge, *Adv. Mater.*, 2025, **37**, 2503954.

9 M. Li, J. Ding, Z. Zhang, Q. Ma, C. Li, M. Lu, H. Zhang, T. Pauporté, W. Mo, J. X. Tang, J. Chen and C. Chen, *Adv. Mater.*, 2025, **37**, 2502729.

10 C. Kim, K. Kim, Y. Kim, N. Tsvetkov, N. J. Jeon, B. J. Kang and H. Min, *Energy Environ. Sci.*, 2024, **17**, 8582–8592.

11 D. Gao, R. Li, X. Chen, C. Chen, C. Wang, B. Zhang, M. Li, X. Shang, X. Yu, S. Gong, T. Pauporté, H. Yang, L. Ding, J. Tang and J. Chen, *Adv. Mater.*, 2023, **35**, 2301028.

12 M. Lu, J. Ding, Q. Ma, Z. Zhang, M. Li, W. Gao, W. Mo, B. Zhang, T. Pauporté, J. Zhang, Y. Wang, J.-X. Tang, J. Chen and C. Chen, *Energy Environ. Sci.*, 2025, **18**, 5973–5984.

13 Y. H. Lin, F. Vikram, F. Yang, X. L. Cao, A. Dasgupta, R. D. J. Oliver, A. M. Ulatowski, M. M. McCarthy, X. Shen, Q. Yuan, M. G. Christoforo, F. S. Y. Yeung, M. B. Johnston, N. K. Noel, L. M. Herz, M. S. Islam and H. J. Snaith, *Science*, 2024, **384**, 767–775.

14 H. Meng, K. Mao, F. Cai, K. Zhang, S. Yuan, T. Li, F. Cao, Z. Su, Z. Zhu, X. Feng, W. Peng, J. Xu, Y. Gao, W. Chen, C. Xiao, X. Wu, M. D. McGehee and J. Xu, *Nat. Energy*, 2024, **9**, 536–547.

15 Y. Zou, W. Yu, B. Qu, Z. Chen, M. Wei and L. Xiao, *Nat. Rev. Mater.*, 2025, **10**, 400–402.

16 Q. Zhang, H. Huang, Y. Yang, M. Wang, S. Qu, Z. Lan, T. Jiang, Z. Wang, S. Du, Y. Lu, Y. Suo, P. Cui and M. Li, *Adv. Mater.*, 2024, **36**, 2410390.

17 X. Li, W. Zhang, X. Guo, C. Lu, J. Wei and J. Fang, *Science*, 2022, **375**, 434–437.

18 C. Li, X. Wang, E. Bi, F. Jiang, S. M. Park, Y. Li, L. Chen, Z. Wang, L. Zeng, H. Chen, Y. Liu, C. R. Grice, A. Abudulimu, J. Chung, Y. Xian, T. Zhu, H. Lai, B. Chen, R. J. Ellingson, F. Fu, D. S. Ginger, Z. Song, E. H. Sargent and Y. Yan, *Science*, 2023, **379**, 690–694.

19 D. Liu, X. Wang, X. Wang, B. Zhang, X. Sun, Z. Li, Z. Shao, S. Mao, L. Wang, G. Cui and S. Pang, *Angew. Chem., Int. Ed.*, 2023, **135**, e202301574.

20 G. Feng, T. Wang, X. He, H. Chen, W. Lu, Z. Zhou, Q. Cao and X. Li, *Nano Energy*, 2025, **141**, 111084.

21 H. Wang, S. Su, Y. Chen, M. Ren, S. Wang, Y. Wang, C. Zhu, Y. Miao, C. Ouyang and Y. Zhao, *Nature*, 2024, **634**, 1091–1095.

22 B. A. Seid, S. Ozen, A. F. Castro-Méndez, D. Neher, M. Stolterfoht and F. Lang, *Adv. Mater.*, 2025, **37**, 2501588.

23 Z. Qu, Z. Zhao, F. Ma, L. Mei, X.-K. Chen, H. Zhou, X. Chu, Y. Yang, Q. Jiang, X. Zhang and J. You, *Nat. Commun.*, 2024, **15**, 8620.

24 C. Liu, Y. Yang, H. Chen, J. Xu, A. Liu, A. S. R. Bati, H. Zhu, L. Grater, S. S. Hadke, C. Huang, V. K. Sangwan, T. Cai, D. Shin, L. X. Chen, M. C. Hersam, C. A. Mirkin, B. Chen,

M. G. Kanatzidis and E. H. Sargent, *Science*, 2023, **382**, 810–815.

25 X. Zhang, S. Jiang, Y. Geng, L. Yang, C. Shen, F. Zhou, Z. Ni, G. Yang and B. Chen, *Adv. Mater.*, 2025, **37**, 2504351.

26 Y. Yang, H. Chen, C. Liu, J. Xu, C. Huang, C. D. Malliakas, H. Wan, A. S. R. Bati, Z. Wang, R. P. Reynolds, I. W. Gilley, S. Kitade, T. E. Wiggins, S. Zeiske, S. Suragtkhuu, M. Batmunkh, L. X. Chen, B. Chen, M. G. Kanatzidis and E. H. Sargent, *Science*, 2024, **386**, 898–902.

27 M. Ebic, F. Sadegh, M. Ans, P. Yadav, D. Prochowicz and S. Akin, *J. Energy Chem.*, 2025, **109**, 120–128.

28 M. Hou, Y. Wang, X. Yang, M. Han, H. Ren, Y. Li, Q. Huang, Y. Ding, Y. Zhao, X. Zhang and G. Hou, *Nano Energy*, 2022, **94**, 106922.

29 S. Song, S. J. Yang, J. Choi, S. G. Han, K. Park, H. Lee, J. Min, S. Ryu and K. Cho, *ACS Appl. Mater. Interfaces*, 2021, **13**, 37052–37062.

30 S. Teale, M. Degani, B. Chen, E. H. Sargent and G. Grancini, *Nat. Energy*, 2024, **9**, 779–792.

31 Y. Li, Y. Zhang, L. Zhang, C. Liu, X. Zhou, D. Wang, B. Niu, C. Lu, J. Chang, X. Jiang, Z. Tang and B. Xu, *Sol. RRL*, 2022, **6**, 2101107.

32 X. Zheng, B. Chen, J. Dai, Y. Fang, Y. Bai, Y. Lin, H. Wei, X. C. Zeng and J. Huang, *Nat. Energy*, 2017, **2**, 17102.

33 Z. Zhang, J. Ding, H. Liu, C. Li, M. Li, T. Pauporté, J. x. Tang, J. Chen and C. Chen, *Adv. Mater.*, 2025, **37**, 2508126.

34 H. Xu, Z. Liang, J. Ye, Y. Zhang, Z. Wang, H. Zhang, C. Wan, G. Xu, J. Zeng, B. Xu, Z. Xiao, T. Kirchartz and X. Pan, *Energy Environ. Sci.*, 2023, **16**, 5792–5804.

35 X. Shi, K. Xu, Y. He, Z. Peng, X. Meng, F. Wan, Y. Zhang, Q. Guo and Y. Chen, *Nano-Micro Lett.*, 2025, **17**, 313.

36 X. Fan, J. Chen, J. Wang, J. Wang, J. Zeng, F. Wei, S. Gao, J. Li, J. Zhang, F. Yan and W. Song, *Energy Environ. Sci.*, 2025, **18**, 2905–2917.

37 K. Wang, Z. Xu, K. Li, R. Li, Z. Guo, Y. Yang, J. Huang, O. F. Mohammed and Z. Zang, *Joule*, 2025, **9**, 102044.

38 C. Sun, L. Jin, X. Wang, B. Shi, P. Wang, N. Ren, X. Han, L. Sun, Z. Zhu, Q. Huang, S. Xu, Y. Zhao, L. Zhang and X. Zhang, *ACS Energy Lett.*, 2025, **10**, 2171–2179.

39 L. Bian, Z. Xin, Y. Zhao, L. Gao, Z. Dou, L. Li, Q. Guo, J. Duan, J. Dou, Y. Wang, X. Zhang, C. Jiang, L. Sun, Q. Zhang and Q. Tang, *J. Energy Chem.*, 2024, **98**, 327–333.

40 L. Yang, C. Yang, W. Wei, J. Weng, J. Lv, M. Zhan, Y. Wei, Z. Tang, X. Zheng and H. Huang, *Angew. Chem., Int. Ed.*, 2025, **64**, e202509065.

41 G. Yang, X. Liu, L. Wang, K. Dong, B. Zhang, X. Jiang, Y. Yin, M. Wang, W. Niu, L. Zheng, S. Yu, S. Liu, S. M. Zakeeruddin, X. Guo, S. Pang, L. Sun, M. Grätzel and M. Wei, *Angew. Chem., Int. Ed.*, 2024, **63**, e202410454.

42 Z. Zhu, B. Ke, K. Sun, C. Jin, Z. Song, R. Jiang, J. Li, S. Kong, C. Liu, S. Bai, S. He, Z. Ge, F. Huang, Y.-B. Cheng and T. Bu, *Energy Environ. Sci.*, 2025, **18**, 4120–4129.

43 D. Wang, Y. Li, W. Li, W. Pan, X. Liu, J. Wu, X. Guo and Q. Li, *Angew. Chem., Int. Ed.*, 2025, **64**, e202509529.

44 M. Yang, T. Zhang, P. Schulz, Z. Li, G. Li, D. H. Kim, N. Guo, J. J. Berry, K. Zhu and Y. Zhao, *Nat. Commun.*, 2016, **7**, 12305.

45 X. He, H. Chen, J. Yang, T. Wang, X. Pu, G. Feng, S. Jia, Y. Bai, Z. Zhou, Q. Cao and X. Li, *Angew. Chem., Int. Ed.*, 2024, **63**, e202412601.

46 X. Wang, C. Zhang, T. Liu, S. Qin, Z. Lin, C. Shi, D. Zhao, Z. Zhao, X. Qin, M. Li and Y. Wang, *Small*, 2024, **20**, 2311673.

47 X. Sun, P. Zhang, T. Liu, B. Tian, P. Xu, Y. Jiang, J. Zhang, Y. Tang, Z. Hu, W. Zhang, Z. Zhang, X. Zhao and W. Guo, *Angew. Chem., Int. Ed.*, 2025, **64**, e202501164.

48 S. Liu, Z. Sun, X. Lei, T. Miao, Q. Zhou, R. Chen, J. Wang, F. Ren, Y. Pan, Y. Cai, Z. Tan, W. Liu, X. Liu, J. Li, Y. Zhang, B. Xu, Z. Liu and W. Chen, *Adv. Mater.*, 2024, **37**, 2415100.

49 Y. Liu, T. Kong, Y. Zhang, Z. Zhao, W. Chen, W. Liu, P. Gao, X. D. Wang and D. Bi, *Adv. Energy Mater.*, 2025, **15**, 2404638.

50 Y. Guo, H. Huang, Y. Zhang, Z. Feng, Y. Wang, J. Xu, H. Zhang, Y. Ji, L. Li, C. Ge, X. Wu, Y. Liu, X. Li, Y. Peng, C. Huang, Y. Zhang, J. Sun, S. Chen, W. Zhou, D. Tang, J. Z. Liu, K. Weber, Y. Li, B. Ding, H. Zhan, X. Zhang and J. Peng, *J. Mater. Chem. A*, 2025, **13**, 26564–26572.

51 W. Zhou, Y. Cai, S. Wan, Y. Li, X. Xiong, F. Zhang, H. Fu and Q. Zheng, *Energy Environ. Sci.*, 2025, **18**, 3828–3838.

52 W. Zhang, C. Duan, M. Du, Z. Cai, P. Cong, C. Li, T. Xue, J. Du, Q. Guo and E. Zhou, *Small*, 2024, **20**, 2407826.

53 X. Li, Z. Ying, L. Liu, J. Wu, H. Ma, Z. He, Y. Yu, Y. Sun, M. Zhang, X. Guo, Y. Zeng, X. Yang and J. Ye, *Nat. Commun.*, 2025, **16**, 8692.

54 G. Hua, X. Lin, Y. Lai, L. Huo, W. Wang and W. Tang, *Adv. Funct. Mater.*, 2024, **35**, 2414423.

55 X. Qiao, R. Zhu, D. Yan, Z. Su, Z. Zhang, H. Wu, Y. Tan, M. Liang, W. Zuo, J. Zhang, G. Li, X. Gao, M. Saliba and M. Li, *Adv. Funct. Mater.*, 2024, **34**, 2409852.

56 E. A. Duijnstee, J. M. Ball, V. M. Le Corre, L. J. A. Koster, H. J. Snaith and J. Lim, *ACS Energy Lett.*, 2020, **5**, 376–384.

57 H. Chen, C. Liu, J. Xu, A. Maxwell, W. Zhou, Y. Yang, Q. Zhou, A. S. R. Bati, H. Wan, Z. Wang, L. Zeng, J. Wang, P. Serles, Y. Liu, S. Teale, Y. Liu, M. I. Saidaminov, M. Li, N. Rolston, S. Hoogland, T. Filleter, M. G. Kanatzidis, B. Chen, Z. Ning and E. H. Sargent, *Science*, 2024, **384**, 189–193.

58 X. Huang, C. Zhang, L. Cao, T. Liu, M. Shen, F. You, Q. Song, G. Feng and C. Liang, *Chem. Eng. J.*, 2025, **511**, 161967.

59 A. O. Alvarez, J. J. de Boer, L. Sonneveld, Y. Bleiji, E. Alarcón-Lladó and B. Ehrler, *ACS Energy Lett.*, 2025, **10**, 3983–3992.

60 Q. Cai, Q. Tan, J. He, S. Tang, Q. Sun, D. He, T. Cheng, G. Ma, J. Huang, G. Su, C. Chen, H. Gu, B. Wang, J. Fan, G. Xing and Z. He, *Joule*, 2025, **9**, 101880.

61 Y. Zhao, X. Luan, L. Han and Y. Wang, *Adv. Funct. Mater.*, 2024, **34**, 2405646.

62 S. Qi, C. Ge, P. Wang, B. Wu, Y. Zhao, R. Zhao, S. Shafian, Y. Hua and L. Xie, *ACS Appl. Mater. Interfaces*, 2024, **16**, 51037–51045.

63 S. S. Khamgaonkar and V. Maheshwari, *Energy Environ. Sci.*, 2025, **18**, 7980–7994.

64 K. Zhao, L. Yao, C. Değer, X. Zhang, J. Shen, X. Miao, P. Shi, Y. Luo, D. Jin, Y. Tian, J. Xu, S. Zhang, Q. Liu, S. Chu, X. Wang, L. Tian, I. Yavuz, J. Xue and R. Wang, *Nat. Commun.*, 2025, **16**, 10074.